

Modeling quasar accretion disc temperature profiles

P. B. Hall^{1*}, E. S. Noordeh¹, L. S. Chajet¹, E. Weiss¹, C. J. Nixon^{2,3}

¹*Department of Physics and Astronomy, York University, Toronto, ON M3J 1P3, Canada*

²*JILA, University of Colorado & NIST, Boulder, CO 80309-0440, USA*

³*Einstein Fellow*

November 28, 2021

ABSTRACT

Micro-lensing observations indicate that quasar accretion discs have half-light radii larger than expected from standard theoretical predictions based on quasar fluxes or black hole masses. Blackburne and colleagues have also found a very weak wavelength dependence of these half-light radii. We consider disc temperature profile models that might match these observations. Nixon and colleagues have suggested that misaligned accretion discs around spinning black holes will be disrupted at radii small enough for the Lense-Thirring torque to overcome the disc’s viscous torque. Gas in precessing annuli torn off a disc will spread radially and intersect with the remaining disc, heating the disc at potentially large radii. However, if the intersection occurs at an angle of more than a degree or so, highly supersonic collisions will shock-heat the gas to a Compton temperature of $T \sim 10^7$ K, and the spectral energy distributions (SEDs) of discs with such shock-heated regions are poor fits to observations of quasar SEDs. Torn discs where heating occurs in intermittent weak shocks that occur whenever the intersection angle reaches a tenth of a degree pose less of a conflict with observations, but do not have significantly larger half-light radii than standard discs. Our toy model for torn accretion discs is therefore unable to simultaneously match observed SEDs and large half-light radii in quasars. We also study two phenomenological disc temperature profile models. We find that discs with a temperature spike at relatively large radii and lowered temperatures at radii inside the spike yield improved and acceptable fits to micro-lensing sizes in most cases. Such temperature profiles could in principle occur in sub-Keplerian discs partially supported by magnetic pressure. However, such discs overpredict the fluxes from quasars studied with micro-lensing except in the limit of negligible continuum emission from radii inside the temperature spike.

Key words: galaxies: nuclei - quasars: general - quasars: absorption lines

1 INTRODUCTION

Standard accretion disc theory (Shakura & Sunyaev 1973; Novikov & Thorne 1973, hereafter SS73 and NT73, respectively) predicts a disc’s effective temperature as a function of radius, from which its half-light radius as a function of wavelength can be calculated. The predicted disc temperature profile is

$$T(R) \propto f_{\text{Edd}}^{1/4} M_{\text{BH}}^{1/2} (R/R_g)^{-3/4} \quad (1)$$

at $R \gg R_g$, where $R_g \equiv GM_{\text{BH}}/c^2$ with M_{BH} the black hole mass and f_{Edd} the quasar’s bolometric luminosity relative to its Eddington luminosity. The corresponding prediction for the variation of the half-light radius with wavelength is

$$R_{1/2} \propto f_{\text{Edd}}^{1/3} M_{\text{BH}}^{2/3} \lambda^{4/3} \quad (2)$$

for a broad range of wavelengths.

Quasar accretion disc half-light radii can be inferred using observations of gravitationally lensed quasars (see, e.g., Wambsganss 2006). Micro-lensing by stars in the lensing galaxy causes the flux ratios of the lensed images to deviate from the predictions of models with smooth mass distributions. The amplitude of these deviations depends on the size of the emission region at the wavelength being observed relative to the typical Einstein radius of the lensing stars.

Observationally, it has been found that quasar accretion discs have *microlensing sizes* (inferred from micro-lensing observations) which are larger than the *theory sizes* (Morgan et al. 2010) predicted from theory given each quasar’s estimated black hole mass and assuming accretion at the Eddington rate, 10% accretion efficiency and an average disc inclination to the line of sight of 60° . In the three studies to date with sample sizes of ten or more objects,

* E-mail: phall@yorku.ca

the microlensing sizes range from a factor of $\sim 1.8 \pm 1.6$ higher on average at mean rest-frame wavelength 2660 Å (Morgan et al. 2010, hereafter M10) to a factor of $\sim 5_{-4}^{+3}$ (Jiménez-Vicente et al. 2012) to $\sim 10_{-5}^{+7}$ (Blackburne et al. 2011, hereafter B11)¹ higher on average at mean rest-frame wavelength 1736 Å.

The above results show that microlensing sizes are larger than theory sizes at only marginal significance (assuming accretion at the Eddington limit, which may be an overestimate; see Kollmeier et al. 2006). However, microlensing sizes are significantly larger than quasar *flux sizes* (M10). Flux sizes are found by determining how large a standard disc would need to be to generate the specific luminosity corresponding to the observed magnification-corrected flux of the quasar at a given wavelength. M10 find that microlensing sizes are $\sim 4 \pm 2$ times larger than flux sizes. Similar results have been obtained in studies of individual objects (e.g., Morgan et al. 2008; Dai et al. 2010; Poindexter & Kochanek 2010; Mediavilla et al. 2011; Morgan et al. 2012).

As for the wavelength dependence of quasar half-light radii, the microlensing sizes in the study of B11 are very weakly dependent on wavelength in ten of eleven cases studied, implying in the simplest case a temperature profile steeply decreasing with radius at temperatures that generate ultraviolet emission. On average, B11 finds $R_{1/2} \propto \lambda^\nu$ with $\nu = 0.17 \pm 0.15 \pm 0.13$ (quoting random and systematic errors), where $\nu = 4/3$ is predicted by theory.

The results of B11 contrast with studies of individual objects which have generally found results consistent with the theoretical prediction: $\nu = 1.64_{-0.42}^{+0.63}$ for HE 1104–1805 (Poindexter et al. 2008); $\nu = 1.48_{-0.43}^{+0.60}$ for MG 0414+0534 (Bate et al. 2008), as compared to $\nu = 1.50 \pm 0.84$ for that object in B11; $\nu = 1.3 \pm 0.3$ for HE 0435–1223 (Mosquera et al. 2011), as compared to $\nu = 0.67 \pm 0.55$ for that object in B11; $\nu = 1.2 \pm 0.3$ for Q 2237+0305 (Eigenbrod et al. 2008); $\nu = 1.0 \pm 0.5$ for SBS 0909+532 (Mediavilla et al. 2011); and $\nu < 4/3$ at 94% confidence for SDSS J0924+0219 (Floyd et al. 2009), as compared to $\nu = 0.17 \pm 0.49$ for that object in B11.

Further studies of microlensed quasars are clearly needed (Mosquera & Kochanek 2011). Meanwhile, investigation of possible explanations for unexpectedly large sizes and nonstandard temperature profiles in quasar accretion discs is warranted.

To summarize: there is marginal evidence that quasar accretion discs are larger than their theory sizes (though the evidence strengthens if quasars are not typically accreting at the Eddington limit), considerable evidence that they are larger than their flux sizes, and possible evidence that their half-light radii have a different wavelength dependence than that predicted by theory. As discussed in M10, a complication to the latter issue is that reconciling the three size measurements may require *flatter* temperature profiles ($\beta < 3/4$) and thus a steeper size-wavelength relation ($\nu = \beta^{-1} > 4/3$). The two constraints are not necessarily contradictory; a nonmonotonic temperature profile

can be locally steep yet effectively flat overall. If the correct temperature profile and physical parameters are used, theory sizes and flux sizes should agree with each other and with the microlensing sizes and the observed wavelength dependence of the sizes should match that predicted by the temperature profile.

Other options discussed in M10 to help explain the three discrepant size measurements include low accretion efficiency for unobscured quasars or increasing the apparent disc size through contamination by line emission arising on larger physical scales or through scattering (Dai et al. 2010, see also). For example, a large fraction of the disc continuum could be intercepted by a strongly warped disc (e.g., Nayakshin 2005; Tremaine & Davis 2013). In that case, the half-light radius will increase with a wavelength dependence related to the disc albedo, as radiation not scattered by the disc will be absorbed and reradiated at the local equilibrium temperature (which will be lower than the characteristic temperature of the continuum emission from smaller radii).

Disc sizes also increase with Eddington ratio, so super-Eddington accretion may also help explain discrepant size measurements. Furthermore, Abolmasov & Shakura (2012) have suggested that the steep temperature profile found by B11 arises from the formation of a scattering photosphere in gas outflowing from the inner regions of an accretion disc undergoing super-Eddington accretion (see also Bonning et al. 2013; Sutton et al. 2013). The small size of the X-ray emitting regions in quasars (e.g., Morgan et al. 2012) could be explained in their model if the outflowing gas forms a Compton-thick funnel-shaped wind and photosphere, so that quasars are only visible within the cone of the funnel because the funnel obscures both the X-ray and UV continuum source regions when viewed from other angles.

Another possible explanation for the temperature profiles found by B11 may arise from changes to an accretion disc resulting from misalignment of its initial angular momentum vector and the angular momentum vector of a spinning black hole.

Any material in the vicinity of a massive spinning object experiences a precession induced by the frame dragging due to the object (Lense & Thirring 1918). The result of this precession, known as the Lense-Thirring effect, on a misaligned disc around the object is that each individual ring in the disc will precess at different rate, warping the disc.

Bardeen & Petterson (1975) showed that the discs around spinning black holes evolve in such a way that in the final configuration the disc is warped, with the orbital angular momentum of the inner region either aligned or anti-aligned with the spin axis of the black hole while the disc's outer region remains unperturbed. Warped-disc dynamics has been the subject of extensive research (e.g., Papaloizou & Pringle 1983; Kumar & Pringle 1985; Pringle 1992; Papaloizou & Lin 1995; Ogilvie 1999; Lubow et al. 2002).

In several recent papers, Nixon and colleagues have suggested that the inner regions of inclined discs could evolve by tearing apart instead of smoothly warping.

Nixon et al. (2012a, hereafter NKPF) showed that for realistic parameters, the inner region of randomly oriented accretion discs around a spinning black hole will tear, due to the Lense-Thirring effect. If the angle between the outer

¹ To calculate this factor for B11, we use their median half-light radii computed with a logarithmic prior and scale to the Eddington ratio and accretion efficiency used by other references.

disc and the black hole spin is in the range $\sim 45^\circ - 135^\circ$, the misalignment between the inner edge of the outer disc and the annulus (of width $\sim H$) torn off it will be $> 90^\circ$ after half a precession period. The rotational velocities of those gas parcels will then be partially opposed, leading to cancellation of angular momentum and rapid infall (see Nixon, King, & Price 2012b). NKPF suggested that, given the smallness of the misalignment angle upper limit for avoiding disc tearing (of order a few degrees), the effect should be common in accretion around the supermassive black holes that power quasars.

When gas in a precessing annulus torn from a disc intersects with gas in an annulus still connected to the disc, the intersecting gas will be collisionally heated. High-temperature gas in intersection regions at relatively large distances from the central black hole can in principle help explain the large, relatively wavelength-independent half-light radii inferred for quasar accretion discs. In addition, the wide range of behaviors possible in the torn disc model as a function of the initial disc-BH spin misalignment angle could in principle help explain the wide range of wavelength dependences in quasar accretion disc half-light radii (Blackburne et al. 2011).

In this paper we examine whether the temperature profiles of torn and other non-standard discs can simultaneously reproduce the observed spectral energy distributions and inferred large half-light radii of quasar accretion discs. In § 2 we outline the initial torn-disc model used in our study. In § 3 we discuss the temperature profiles and SEDs for selected torn discs. In § 4 we explore a small set of additional temperature profiles. We discuss our results in § 5. Where necessary, we assume a flat universe with $\Omega_M = 0.3$, $\Omega_\Lambda = 0.7$, and $H_0 = 70 \text{ km s}^{-1} \text{ Mpc}^{-1}$.

2 TORN DISC TOY MODEL

Our initial model begins with accreting material forming a Keplerian disc at large radii from the black hole. The disc's spin axis is oriented at a random angle $0^\circ < \theta < 180^\circ$ relative to the black hole spin axis.

The disc spreads inwards and different annuli in it precess at different rates due to the Lense-Thirring effect, so the disc warps as it spreads inwards.

The disc eventually reaches a radius where viscous dissipation cannot overcome the shear between adjacent annuli imposed by the Lense-Thirring effect.

The innermost annulus of the disc then tears away from the rest of the disc and precesses independently. This annulus has width $\sim H$, where H is the local disc height.

There will be two contact points between the precessing annulus and the next innermost annulus (which forms the inner edge of the outer disc). At these points gas from each annulus on intersecting orbits is likely to shock, converting some orbital motion to heat. The post-shock gas will be unable to remain in circular orbits at the intersection radius. The original NKPF picture consists of gas intersecting at angles up to 2θ .

2.1 Break radius and circularization radius

The disc tears at a break radius R_b given by Eq. 7 and Eq. 8 of NKPF:

$$R_b(\theta) \lesssim \left(\frac{4}{3} |\sin \theta| \frac{a}{\alpha} \frac{R}{2H}\right)^{2/3} R_g \quad (3)$$

$$R_b(\theta) \lesssim 350 R_g |\sin \theta|^{2/3} \left(\frac{a}{0.5}\right)^{2/3} \left(\frac{\alpha}{0.1}\right)^{-2/3} \left(\frac{2H/R_b}{10^{-3}}\right)^{-2/3} \quad (4)$$

where $2H$ instead of H appears in the above equations because we use H to refer to the disc scale height, whereas NKPF use it to refer to the disc thickness.

Gas which precesses and intersects at R_b loses angular momentum, meaning that it can recircularize its orbit only at some circularization radius $R_{circ} < R_b$. Nixon et al. (2012b) give an approximate expression for R_{circ} (their Eq. 3), but the exact expression for the circularization radius of an annulus of width H centered at $R_b - H/2$ and an annulus of width H centered at $R_b + H/2$, intersecting at an angle 2θ is

$$\frac{R_{circ}(\theta)}{R_b(\theta)} = \frac{1}{2} + \frac{1}{2} \sqrt{1 - \left(\frac{H}{2R_b}\right)^2 \cos(2\theta)}. \quad (5)$$

Note that the above is the minimum possible R_{circ} ; if gas intersects at angle $\eta < 2\theta$, it will circularize at an intermediate radius $R_{circ} < R < R_b$.

2.2 Shock heating

When an annulus torn off a disc oriented at angle θ to the black hole spin precesses, its intersection angle with the adjacent annulus that forms the inner edge of the outer disc will cycle sinusoidally between 0 and 2θ . The intersection angle between these annuli as a function of time, $\eta(t)$, is given by

$$\begin{aligned} \eta(t) &= 2\theta \times |\sin(180^\circ t/t_p)| & 0^\circ < \theta < 90^\circ \\ \eta(t) &= (360^\circ - 2\theta) \times |\sin(180^\circ t/t_p)| & 90^\circ < \theta < 180^\circ \end{aligned} \quad (6)$$

where the precession period is $t_p = 360^\circ/\Omega_p$, with Ω_p the Lense-Thirring precession frequency in degrees per unit time.

At each intersection, each annulus approaches at an angle $\eta/2$ to their mutual bisector. We assume that the kinetic energy from motion transverse to the bisector is converted into thermal energy. This kinetic energy is $K = 2 \times \frac{1}{2} (N \mu m_H) [v_K \sin(\eta/2)]^2$, where N is the number of particles (of mean mass μm_H) in each annulus and v_K is the Keplerian velocity at the intersection radius. If all this transverse kinetic energy is converted to heat, the resulting thermal energy is distributed among the same $2N$ particles: $E = \frac{3}{2} (2N) k_b \Delta T$, where ΔT is the temperature increase of the gas. Thus, for gas intersecting at angle η at radius $R_b(\theta)$,

$$\Delta T = \frac{\mu m_H}{3k_b} [v_K(R_b(\theta))]^2 \sin^2 \frac{\eta}{2}. \quad (7)$$

This ΔT forms an additional term for the surface temperature T_{surf} in a region of width $H(R_b)$ wherever a precessing annulus is present.

If gas is shock-heated to a temperature higher than the

Compton temperature of the ambient radiation field, the gas will cool by transferring its thermal energy to the radiation field through inverse Compton scattering. The Compton temperature of a quasar radiation field is $\sim 10^7$ K (Eq. 25 and 26 of Sazonov et al. 2004). We therefore cap the value of T_{surf} at 10^7 K.

3 TORN DISC TOY MODEL SEDS AND HALF-LIGHT RADII

The temperature profile and SED of a torn disc ultimately depend on the disc/BH spin misalignment angle θ , the dimensionless BH spin parameter a ($0 \leq a \leq 1$), the dimensionless viscosity parameter α , the disc height to radial distance ratio H/R , and the black hole mass M_{BH} and normalized mass accretion rate $\dot{M}c^2/L_{\text{Edd}} \propto \dot{M}/M_{\text{BH}}$. B11 write this latter quantity as f_{Edd}/η , where the Eddington ratio is $f_{\text{Edd}} = L_{\text{bol}}/L_{\text{Edd}} = \dot{M}/\dot{M}_{\text{Edd}}$ and the accretion efficiency is $\eta = L_{\text{bol}}/\dot{M}c^2$. B11 assumed $\eta = 0.15$ and $f_{\text{Edd}} = 0.25$, whereas in all cases we assume a Schwarzschild black hole ($\eta = 0.057$). To match the value of f_{Edd}/η used by B11, we assume $f_{\text{Edd}} = 0.1$. We also assume $H/R = 1.7 \times 10^{-3}$ (so that the disc height at any radius is $H = 1.7 \times 10^{-3}R$), $\alpha = 0.1$, and $M_{\text{BH}} = 10^9 M_{\odot}$. In our illustrative calculations below, we adopt a SS73 temperature profile (valid only for $a = 0$) even for the case of $a \neq 0$, as our arguments are insensitive to the differences between SS73 and NT73 SEDs.

3.1 Single- R_b case

Equations 4, 5 and 7 generate a family of temperature profiles as a function of θ which consist of:

- a normal SS73 disc ($T_{\text{surf}} = T_{\text{SS73}}$) at $R < R_{\text{circ}}(\theta)$,
- a gap at $R_{\text{circ}} < R < R_b(\theta) - H(R_b)$,
- a shock-heated region ($T_{\text{surf}} = T_{\text{SS73}} + \Delta T$) at radii $R_b - H(R_b) < R < R_b + H(R_b)$,
- and a normal SS73 disc again at $R > R_b + H(R_b)$.

To find the temperature profile for the scenario put forth by NKPF, in which the precessing disc intersects with its neighboring annulus over half to one precession periods, for a given θ we use Eq. 7 to calculate $T_{\text{surf}}(R_b) = T_{\text{SS73}}(R_b) + \Delta T(R_b)$ for $\eta = \theta$ ($\theta \leq 90^\circ$) or $\eta = 180^\circ - \theta$ ($\theta \geq 90^\circ$), as the average of η over one precession period is about half the maximum η .

We then calculate spectral energy distributions (SEDs) and half-light radii using the L_{λ} values from the regions $R < R_{\text{circ}}$, $R_b - H < R < R_b + H$ and $R > R_b + H$.

Figure 1 shows an SS73 disc SED and the SEDs resulting from these shock-heated disc temperature profiles. The SEDs are much bluer and more X-ray luminous than observed quasar SEDs. (Note that the SS73 disc model is known to be a poor fit to observations at $\lambda \lesssim 1000 \text{ \AA}$, and that at X-ray wavelengths an additional power-law component is needed in addition to thermal disc emission. Those wavelengths are plotted here to examine if an SED overpredicts the short-wavelength emission, not in expectation of a good fit at short wavelengths from any SED, even a baseline SS73 one.)

We have assumed that an entire annulus at R_b is at the post-shock temperature, but it may be more accurate to assume that only the two intersection regions of surface

area $(2H)^2$ on each face of the disc are at that temperature. Figure 2 shows the SEDs in that case; they are still much bluer and more X-ray luminous than observed quasar SEDs.

We discuss the half-light radii results for this and the next model in § 3.3.

3.2 Small- η case

Large intersection angles between the precessing annulus and the outer disc lead to high-temperature shock-heated regions and SEDs which are inconsistent with observations. A more plausible alternative picture is one in which the intersection angle never becomes large.

As the annulus at R_b starts precessing, the intersection angle between it and the next annulus out will grow with time. The relative velocity between those annuli will also grow with time. Shock heating between the two annuli will happen once the magnitude of their relative velocity is sufficiently large, rather than at the maximum relative velocity possible for that value of θ . Therefore, the relative velocity at the time of intersection may not depend on θ , and the shock-heated temperature may be considerably lower than 10^7 K.

The intersection angle between these two annuli as a function of time, $\eta(t)$, is given by Equation 6. The magnitude of the relative velocity between two annuli at R_b divided by the speed of sound at R_b , $c_s = (H/R_b)v_K$, is given, for $0^\circ < \theta < 90^\circ$, by

$$\frac{v_{\text{rel}}(R_b)}{c_s(R_b)} = \frac{2v_K(R_b)}{[H/R_b]v_K(R_b)} \sin\left[\frac{1}{2}\eta(t)\right] = \frac{2R_b}{H} \sin\left[\frac{1}{2}\eta(t)\right] \quad (8)$$

Setting $v_{\text{rel}}/c_s = 1$ and solving, we find that the value of η at which intersecting annuli will shock is $\eta \simeq 0.1^\circ$.

We now imagine a different scenario for a disc oriented at θ . An annulus breaks off at $R_b(\theta)$, precesses by $\eta = 0.1^\circ$, shocks, and reorients itself and its adjacent annulus to $\theta - 0.05^\circ$. Part of this reoriented annulus will be subject to breaking at $R_b(\theta - 0.05^\circ)$, as the separation between the two break radii will be less than H for most θ .

We suppose that material flows to smaller radii through a number $\theta/0.05^\circ$ of these weak shocks. Each shock heats the disc in two intersection regions of surface area $(2H)^2$ on each face of the disc. Each pair of regions will form at some radius $R_b(\theta_x)$ at the inner edge of part of the disc oriented at some angle θ_x , and the disc material will flow through one or the other of the regions in half an orbital time. Thus, each shock exists only for a time of $\frac{1}{2}t_{\text{orb}}/t_{\text{rad}}$, where t_{rad} is the time it takes material to flow from $R_b(\theta_x)$ to $R_b(\theta_x - 0.05^\circ)$ in an SS73 disc. We compute the average SED expected for such a disc by setting the shock-heated regions' radial widths to $w(R)$, where $2\pi R w \equiv 2(2H)^2 \times \frac{1}{2}t_{\text{orb}}/t_{\text{rad}}$. The shock-heated temperature in each region is

$$\delta T(\theta_x) = \frac{\mu m_H}{3k_b} [v_K(R_b(\theta_x))]^2 \sin^2(0.05^\circ). \quad (9)$$

The average SEDs of discs in this ‘‘small- η ’’ scenario are shown in Figure 3 for the case $\theta = 5^\circ$ and in Figure 4 for the case $\theta = 90^\circ$. In both cases, the average SEDs for $a = 1$ are consistent with observational constraints, while those for $a = 0.1$ are not consistent at sufficiently large θ . This somewhat counterintuitive behaviour arises mainly from the fact that R_b increases with a (Eq. 4). In the small- η scenario,

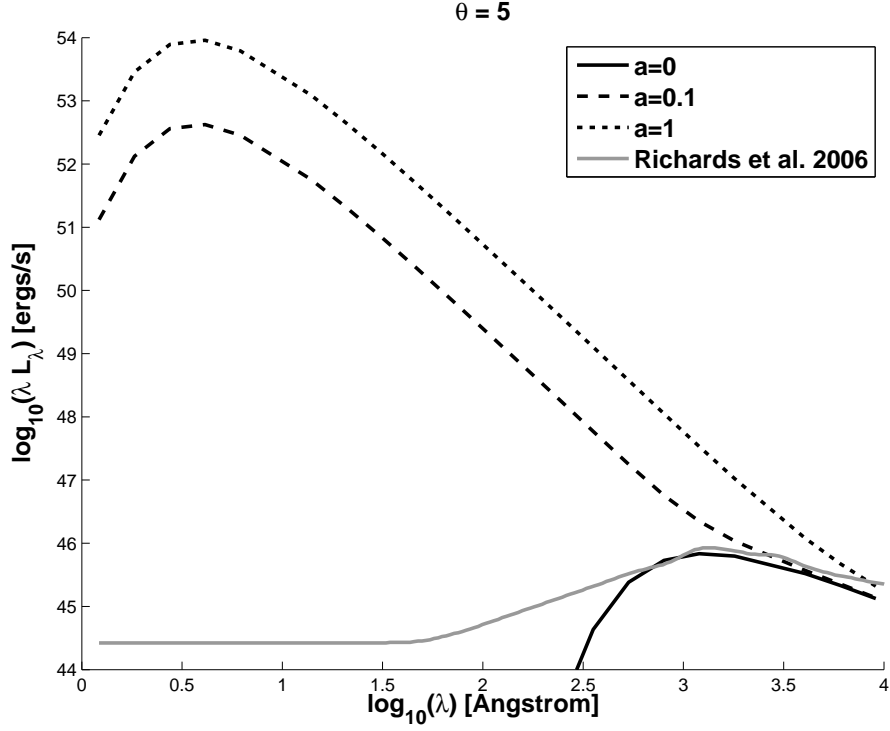


Figure 1. SEDs of accretion discs with $M_{BH} = 10^9 M_{\odot}$ and $f_{Edd}=0.1$. The solid black line is the SED of an accretion disc with $a = 0$. The dashed and dotted lines show the SEDs of discs tilted by $\theta = 5^{\circ}$ from the spin axis of black holes with $a = 0.1$ and 1, respectively, that tear and shock-heat to $T = 10^7$ K at R_b over an annulus of width $2H(R_b)$. The grey line is the mean quasar SED from Richards et al. (2006).

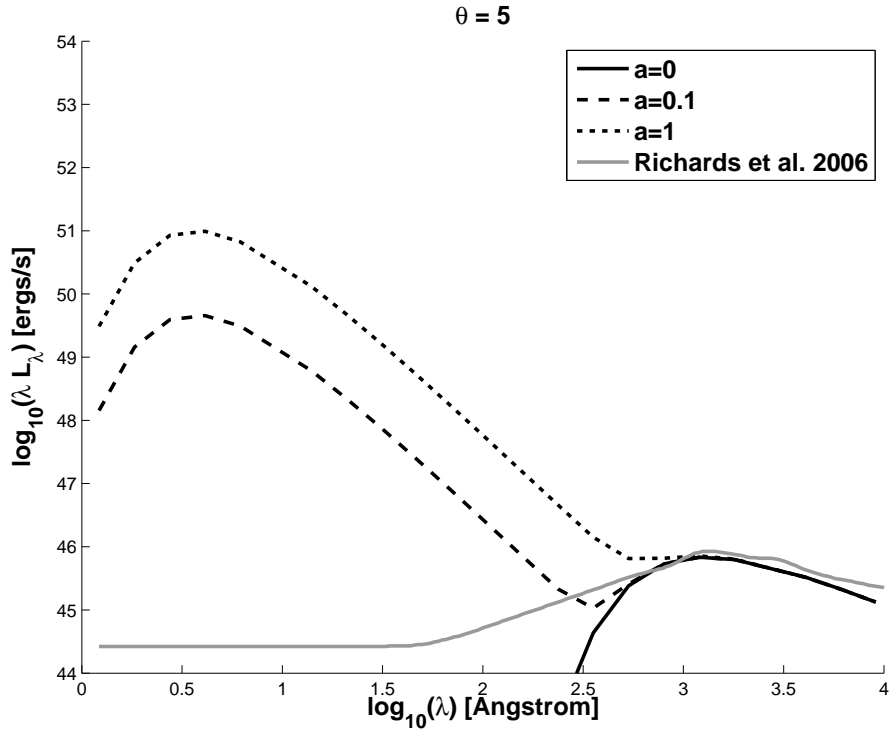


Figure 2. Same as Figure 1, except that shock heating occurs only in the intersecting regions of the torn annulus and the adjacent annulus that forms the inner region of the outer disc.

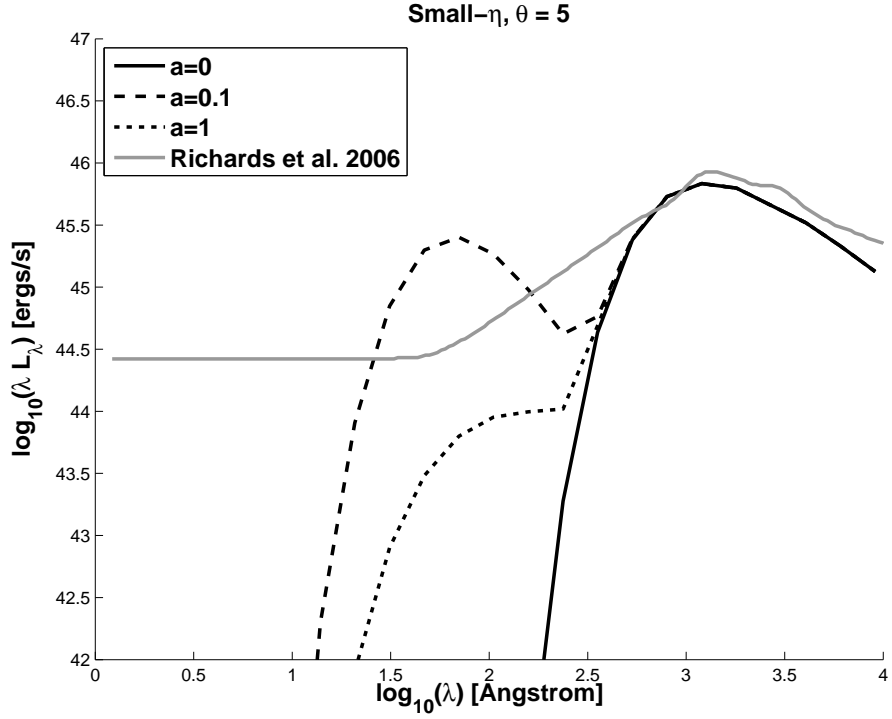


Figure 3. The solid black line is the SED of an accretion disc with $a = 0$. The dashed and dotted lines show the SEDs of discs tilted by $\theta = 5^\circ$ from the spin axis of black holes with $a = 0.1$ and 1 , respectively, that tear and shock-heat in multiple, short-lived shocks, each with intersection angle $\eta = 0.1^\circ$. See § 3.2 for a discussion of why the $a = 1$ curve and not the $a = 0.1$ curve is most similar to the $a = 0$ curve. The grey line is the mean quasar SED from Richards et al. (2006).

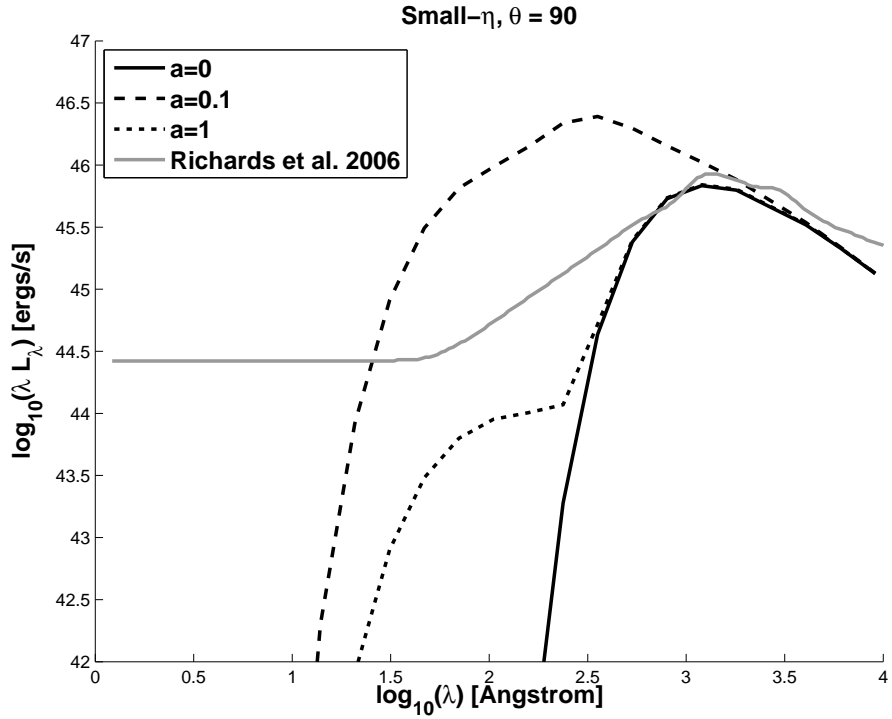


Figure 4. Same as Figure 3, except for $\theta = 90^\circ$.

Table 1. Model accretion disc half-light radii at $\lambda=1736 \text{ \AA}$

Model	Shocked Region	a	$\theta(^{\circ})$	$\log(r_{1/2}$ in cm)
Inferred (B11)	15.97–16.61
SS73	None	0	...	15.55
Single- R_b torn disc	Full Annulus	0.1	5	15.19
Single- R_b torn disc	Full Annulus	0.1	90	15.90
Single- R_b torn disc	Full Annulus	1	5	15.86
Single- R_b torn disc	Full Annulus	1	90	16.56
Single- R_b torn disc	Intersections Only	0.1	5	15.55
Single- R_b torn disc	Intersections Only	0.1	90	15.98
Single- R_b torn disc	Intersections Only	1	5	15.56
Single- R_b torn disc	Intersections Only	1	90	16.56
Small- η torn disc	Intersections Only	0.1	90	15.64
Small- η torn disc	Intersections Only	0.3	90	15.59
Small- η torn disc	Intersections Only	1	90	15.56

The B11 range of $\log(r_{1/2})$ comes from the four objects with masses closest to $M_{BH} = 10^9 M_{\odot}$. SS73, single- R_b and small- η models assume $M_{BH} = 10^9 M_{\odot}$ and $f_{\text{Edd}}=0.1$.

shock locations are at smaller radii and are more closely spaced for $a = 0.1$ than for $a = 1$. Because both the shock-heating temperature increment δT and $T_{\text{surf}} = T_{\text{SS73}} + \delta T$ increase with decreasing radius and we assume the disc is optically thick ($L \propto T^4$), the shock-generated luminosity is larger for smaller a . (This increase does stop at very small a , at which large values of θ are required for shocks to occur at radii larger than the innermost stable circular orbit at which a disc can exist.)

Note that the SEDs in the small- η scenario could in principle be consistent with the range of observed quasar SEDs if most black holes are rapidly spinning, so that cases with $a \gg 0.1$ in Figures 3 and 4 were much more common than cases with $a \lesssim 0.1$. (The first test of that possibility would be to see if the SEDs are relatively unchanged when calculated assuming an NT73 disc with the appropriate value of a instead of an SS73 disc.) However, the SEDs predicted for low spins ($a \approx 0.1$; consistent with the accretion picture of King & Pringle 2006, 2007) do show a soft X-ray component which has recently been shown to be ubiquitous in type 1 AGN (Scott et al. 2012).

3.3 Torn disc toy model results

Table 1 gives the half-light radii at $\lambda = 1736 \text{ \AA}$ inferred by B11 (microlensing sizes) and calculated for the scenarios considered in this section (theory sizes), all for quasars of mass $M_{BH} \simeq 10^9 M_{\odot}$.

Most torn disc cases have larger half-light radii than the SS73 case. However, only the single- R_b , $a = 1$, $\theta = 90^{\circ}$ torn disc cases (with a shocked region over the full annulus or at the intersections only) have half-light radii large enough to match the observationally inferred results of B11. Within the uncertainties, single- R_b torn discs with full-annulus shocked regions around black holes with $a = 1$ might match the observed range of $r_{1/2}$ for a reasonable distribution of angles θ . However, those scenarios do not produce SEDs consistent with observations. And while the small- η scenarios are consistent with observed SEDs for certain parameter choices, none of those scenarios result in half-light radii large enough

to match the observations when averaged over a reasonable range of θ values.

These conclusions hold if f_{Edd} is increased from 0.1 to 1.0. In that scenario the temperature of the disc will be higher at all radii (Eq. 1), increasing $\log(r_{1/2})$ by 0.33 in the SS73 case (Eq. 2), which reduces but does not eliminate the size discrepancy. However, because H/R increases with f_{Edd} (SS73 Eq. 2.8), the values of R_b for torn discs will shrink as f_{Edd} increases (Eq. 4). That will lead to smaller values of $\log(r_{1/2})$ for torn discs in cases where the shocked region dominates the emitted flux and values of $\log(r_{1/2})$ only 0.33 higher in most other cases.

4 PHENOMENOLOGICAL MODEL TESTS

In this section we consider whether better matches to observations can be obtained with two phenomenological models for disc temperature profiles that do not involve torn discs. These models are energetically plausible but are not rigorously derived; our intention is simply to explore how well simple combinations of an underlying disc and a temperature spike can match observations.

We consider the constraints placed on these two phenomenological models by the quasar accretion disc half-light radii inferred by B11 (microlensing sizes; see § 1). B11 characterize the half-light radius' dependence on wavelength in their sample as $r_{1/2} = \lambda^{\nu}$, with $\nu = 0.17 \pm 0.15$. The quantity ν is related to the slope β of a disc temperature profile $T(R) \propto R^{-\beta}$ as $\beta = \nu^{-1}$; thus, B11 constrain $\beta \simeq 6_{-3}^{+8}$.

The weak dependence of the half-light radii on wavelength seen by B11 extends over the wavelength range $0.1 - 1 \mu\text{m}$, corresponding to wavelengths of light emitted by blackbodies at temperatures of approximately $3,000 \text{ K} < T < 30,000 \text{ K}$.

Therefore, one simple explanation for the results of B11 is that quasar accretion discs contain a region where the temperature drops from $T \gtrsim 30,000 \text{ K}$ to $T \lesssim 3,000 \text{ K}$

following a power-law of the approximate form $T(R) \propto R^{-\beta}$ with $\beta \simeq (6_{-3}^{+\infty})$.²

We parametrize our models in terms of M_{BH} (fixed for each quasar), the Eddington ratio f_{Edd} (for which we test a wide range of values), and other parameters appropriate to each of the two models we now present.

4.1 Forming disc model

One possibility for generating higher temperatures at larger radii might be a fragmented disc transitioning to a continuous disc. Goodman (2003) has argued that quasar accretion discs are likely to be unstable against fragmentation due to self-gravity at large radii. If the gas in such a disc is distributed in clumps over some range of radii, random collisions between those clumps will occur at higher velocities at smaller radii within that range. The clumps will survive only down to a radius at which collisions disrupt them enough to establish a continuous disc, and a temperature spike due to collisional heating is plausible near that radius. This radius must be smaller than the maximum radius at which the disc is stable against fragmentation, r_Q .

$$r_Q \simeq 415 \alpha_{0.01}^{14/27} (f_{\text{Edd}}/\eta)^{-8/27} \hat{\kappa}^{2/9} M_8^{-26/27} R_{\text{Sch}} \quad (10)$$

where $1 \lesssim \hat{\kappa} \lesssim 10$ is the opacity relative to the electron scattering opacity and M_8 is the black hole mass in units of $10^8 M_\odot$. We assume $\alpha_{0.01} = 10$ and $\hat{\kappa} = 10$, yielding

$$r_Q \simeq 2292 (f_{\text{Edd}}/\eta)^{-8/27} M_8^{-26/27} R_{\text{Sch}}. \quad (11)$$

In Table 2, for each quasar in B11 we compare its value of r_Q (assuming $f_{\text{Edd}}/\eta = 5/3$, to match B11) to its measured $\langle r_{1/2} \rangle$, where the average is over all wavelengths at which $r_{1/2}$ is measured by B11. The values of r_Q are all larger than the inferred $\langle r_{1/2} \rangle$, indicating that a model with a temperature spike at $r \simeq r_Q$ might be able to match the observations.

We refer to this as our ‘forming disc’ model, in which a smooth disc is continuously forming out of a fragmented disc at R_b . (We do not mean to imply that the disc is necessarily young.) If we denote the temperature profile of an SS73 disc as $T_{\text{SS73}}(R)$ then for the same parameters the temperature profile of the forming disc model $T_{fd}(R)$ is:

$$\begin{aligned} T_{fd}(R < R_b) &= T_{\text{SS73}}(R) \\ T_{fd}(R \geq R_b) &= T_{hi}(R/R_b)^{-\beta}. \end{aligned} \quad (12)$$

For each quasar, this model has one fixed parameter (M_{BH}) and four free parameters: f_{Edd} , the spike temperature T_{hi} , the spike radius R_b (at which the temperature jumps to T_{hi} from some temperature T_{lo}), and the slope β with which the temperature declines at $R > R_b$.

The values these parameters can take are constrained

by energy conservation. The energy per second emitted from the disc in its forming region ($R > R_b$) must be no more than the energy available to the mass per second which has reached that radius from infinity. Consider the limiting case of the forming disc model consists of gas falling radially inward in the disc plane until it reaches R_b , at which point it circularizes onto the inner disc with kinetic energy per unit mass $\frac{1}{2}v^2 = \frac{1}{2}GM_{BH}/R_b$. The potential energy per unit mass gained by reaching R_b is GM_{BH}/R_b . Thus, the forming region of the disc ($R > R_b$) can emit energy at a rate $L \leq \frac{1}{2}GM_{BH}\dot{M}/R_b$, with the characteristic width and peak temperature of the extraction region dependent on β .

In appendix A, we use the above constraint to derive an expression relating the free parameters of this model for $\beta > \frac{1}{2}$:

$$\sigma_{sb} T_{hi}^4 \leq \left[\beta - \frac{1}{2} \right] \frac{GM_{BH}\dot{M}}{2\pi R_b^3} \quad (13)$$

which is in addition to the constraint $R_b \leq r_Q$, with r_Q given by Equation 11). We only consider combinations of parameters that satisfy those constraints.

For this model we test values of β from 1 to 18, f_{Edd} from 0.01 to 1, T_{hi} from 10000 K to 70000 K, and $R_b = R(T_{lo})$ with T_{lo} from 4000 K $< T_{lo} < 28000$ K. We detail our results on this and the next model in § 4.4.

4.2 Magnetically restrained disc models

A disc will have greater viscous dissipation (and thus higher temperatures) than a Keplerian disc if gas flowing inward through a disc has a rate of change of azimuthal speed with radius whose absolute magnitude is greater than that experienced in a Keplerian disc. If the magnitude of the rate of change in azimuthal speed is less than in the Keplerian case, the annulus will have a lower temperature than in the Keplerian case.

Both situations can occur (at different radii) in discs where magnetic pressure is important. Ogilvie (1997) has shown that a disc threaded by a strong poloidal magnetic field can have an angular velocity with order unity deviations from the Keplerian value. In the magnetically arrested disc model of Narayan et al. (2003), a strong poloidal magnetic field disrupts disc accretion at some radius, inside of which gas accretes at much less than the free-fall velocity. We consider a range of ‘magnetically restrained’ models where gas accreting through a Keplerian disc at large radii reduces its orbital velocity to a fraction $f < 1$ of the circular velocity at R_b by the time it reaches radius R_b (increasing the local disc temperature in the process) and continues to orbit at a fraction f of the Keplerian velocity at $R < R_b$. (Sub-Keplerian rotation is required in the inner region to ensure that gas moves inward at R_b instead of being flung outward.) Assuming that the radial velocities in the disc at $R < R_b$ are still much less than the rotational velocities, the sub-Keplerian rotation reduces the dissipational heating at $R < R_b$, leading to temperatures at $R < R_b$ which are \sqrt{f} times the temperatures in an SS73 disc with the same parameters. The combined profile has a cooler inner disc and warmer outer disc than in the forming disc model.

Again denoting the temperature profile of an SS73 disc as $T_{\text{SS73}}(R)$, for the same parameters the temperature pro-

² Other explanations are possible. The locally inhomogeneous accretion disc model of Dexter & Agol (2011) explains large half-light radii, but not their lack of wavelength dependence. A modified inhomogeneous disc model in which regions of the disc flare to some constant temperature $T \gtrsim 30,000$ K within a relatively large radius, but not outside that radius, might explain both trends. However, as we can see no obvious mechanism for generating a radially constant peak flare temperature less than the Compton temperature, we have chosen to explore other models here.

Table 2. Tabulated and derived parameters for quasars from Blackburne et al. (2011)

Quasar	M_{BH} ($10^9 M_\odot$)	$L_{bol,opt}$ (10^{46} erg s $^{-1}$)	$\sigma(\log L_{bol,opt})$ (log erg s $^{-1}$)	Measured $\log\langle r_{1/2} \rangle$ (cm)	$\log(r_Q)$ (cm)	SS73 $\log\langle r_{1/2} \rangle$ (cm)	$\log(r_I)$, $\beta = 3/4$ (cm)	$\log(r_I)$, MR best-fit (cm)	σ_r/σ
HE 0230–2130	0.092	0.29	0.24	16.57	16.76	15.13	14.73	16.73	0.148
MG J0414+0534	1.82	3.6	0.17	15.94	16.81	16.05	14.28	14.38	0.278
HE 0435–1223	0.50	0.38	0.26	16.07	16.79	15.72	14.95	15.11	0.390
RX J0911+0551	0.80	1.3	0.18	16.19	16.80	15.69	14.86	15.12	0.324
SDSS J0924+0219	0.11	0.06	0.56	15.73	16.77	15.30	14.64	14.88	0.530
HE 1113–0641	0.087	0.27	0.26	15.82	16.76	15.34	14.76	14.86	0.997
PG 1115+080	1.23	1.1	0.37	16.69	16.81	15.99	15.21	15.59	0.626
RX J1131–1231	0.06	0.08	0.19	15.51	16.76	15.36	14.88	14.94	0.342
SDSS J1138+0314	0.04	0.38	0.26	15.98	16.75	14.83	14.64	14.90	0.944
SDSS J1330+1810	1.5	4.7	...	16.13	16.81	16.12	14.24
WFI J2026–4536	0.79	2.5	0.26	16.42	16.80	15.77	15.03	15.29	0.474
WFI J2033–4723	0.18	0.57	0.12	16.69	16.77	15.42	14.90	15.16	0.508

Values of M_{BH} and $L_{bol,opt}$ are taken from Table 8 of B11. Uncertainties on $L_{bol,opt}$ are discussed in § 4.3. The measured $\log\langle r_{1/2} \rangle$ column gives the average of each object’s log-prior, median $r_{1/2}$ values from B11. The r_Q values are discussed in § 4.1. The SS73 $\langle r_{1/2} \rangle$ calculations used $f_{Edd} = 0.1$ to match B11 given our assumed value of η (see § 3). The r_I flux sizes are discussed in § 4.4, for both the $\beta = 3/4$ case and the best-fit magnetically restrained (MR) model. The σ_r/σ values are discussed in § 4.3.

file of a magnetically restrained disc model $T_{mr}(R)$ is:

$$\begin{aligned}
 T_{mr}(R < R_b) &= \sqrt{f} T_{SS73}(R) \\
 T_{mr}(R_b \leq R \leq R_c) &= T_{hi}(R/R_b)^{-\beta} \\
 T_{mr}(R \geq R_c) &= T_{SS73}(R)
 \end{aligned} \tag{14}$$

where R_c is defined via $T_{hi}(R_c/R_b)^{-\beta} \equiv T_{SS73}(R_c)$. For each quasar, this model has one fixed parameter, M_{BH} , and five free parameters: f_{Edd} , T_{hi} , R_b (or, equivalently, T_{lo}), β and f .

The values of these parameters are constrained by the fact that the disc has a fraction $(1 - f^2)$ of the kinetic energy of the accreting gas at R_b available to emit as heat at $R > R_b$, in addition to the normal disc emission ($\propto T_{SS73}^4$) at $R > R_b$. We derive the relationship between the parameters of this model in appendix B (equation B5), and require all combinations of parameters we test to satisfy that relationship.

For these magnetically restrained models we test the same parameter space of f_{Edd} , T_{hi} , R_b and β used for the forming disc model, plus values of f given by $f = 0$ and $f = 0.01n^2$ for $n = 2$ to $n = 9$. We detail our results on this and the previous model in § 4.4.

4.3 Random and systematic errors

For each quasar in B11, for a specific model and set of model parameters including that quasar’s M_{BH} we calculate half-light radii at the observed wavelengths and a bolometric luminosity at $\lambda < 1 \mu\text{m}$. We then calculate the χ^2 value of the model using the model and observed $\log L_{bol,opt}$ values from Pooley et al. (2007) and B11 and the model and inferred half-light radii. Most quasars have their half-light radius measured at eight wavelengths; thus, the half-light radius has eight times greater weight in the χ^2 calculation than $L_{bol,opt}$ does.

Inspection of Fig. 6 of B11 shows that the error bars for a given object are generally larger than the scatter between points. Using those error bars would lead to misleadingly small χ^2 and χ^2_ν values. The σ values used in Fig. 6 of

B11 incorporate both random and systematic error, added together in quadrature as $\sigma = \sqrt{\sigma_r^2 + \sigma_s^2}$. Adding random and systematic errors together can lead to erroneous results, but is likely an adequate approximation in this case. The systematic errors considered by B11 were apparent flux ratio deviations arising from emission-line contamination of the observed magnitudes, confusion with adjacent objects on the images, and variability from time delays. Only the latter source of uncertainty is likely to systematically bias the half-light radii at all wavelengths in the same direction; emission-line contamination will vary between filters, and confusion with adjacent objects will vary with the color of the objects. While we first consider only σ_r in our χ^2 calculations, we also show the results of a conservative approach in which we consider the full σ .

To calculate the σ_r values, we assume that each quasar’s total error in $r_{1/2}$ in each filter (Table 7 of B11) can be broken down into random and systematic errors, in proportion to the contribution of random and systematic errors to the uncertainties for all data points for that quasar (Table 5 of B11). From the ratio σ_r/σ_s we determine the ratio σ_r/σ for each quasar (Table 2). The $r_{1/2}$ error values used in our χ^2 calculations are the quasar’s uncertainties σ from Table 7 of B11 multiplied by the quasar’s ratio σ_r/σ from Table 2.

The $\log L_{bol,opt}$ error value used in our χ^2 calculations, $\sigma(\log L_{bol,opt})$, is also tabulated for each quasar in Table 2. For quasars in Pooley et al. (2007), the $\sigma(\log L_{bol,opt})$ values here equal the $\sigma(\log M_{BH})$ there; otherwise, we used the average $\sigma(\log M_{BH}) = 0.26$ from Pooley et al. (2007) as a representative error on $\log L_{bol,opt}$. We do not attempt to separate random and systematic errors on $L_{bol,opt}$.

4.4 Phenomenological model results

For each quasar we calculate a temperature profile for all allowable combinations of the specified parameter values given for each model above. For each model — SS73, forming disc, and magnetically restrained for values of f from 0 to 0.81 — we find the minimum χ^2 value over all tested values of f_{Edd} ,

Table 3. χ^2_{min} results

Quasar	Parameter	SS73	Forming Disc	Magnetically Restrained (f value, κ_λ value)
HE 0230–2130	χ^2_{min}	6176.1	6196.9	235.5 ($f = 0, \kappa_\lambda = 0.0001$)
	f_{Edd}	1	1	1
	$L_{bol,opt}$ (10^{46} erg s $^{-1}$)	1.051	1.057	0.003
	β		12	2
	T_{hi} (K)		15000	5000
	T_{lo} (K)		8000	4000
MG J0414+0534	χ^2_{min}	20.1	20.0	15.1 ($f = 0.09, \kappa_\lambda = 0.6299$)
	f_{Edd}	0.07	0.08	0.03
	$L_{bol,opt}$	1.368	1.484	1.036
	β		1	3
	T_{hi}		10000	60000
	T_{lo}		10000	28000
HE 0435–1223	χ^2_{min}	30.7	29.1	0.9 ($f = 0.25, \kappa_\lambda = 0.4841$)
	f_{Edd}	0.7	0.8	0.4
	$L_{bol,opt}$	3.972	4.532	0.423
	β		6	18
	T_{hi}		10000	30000
	T_{lo}		6000	16000
RX J0911+0551	χ^2_{min}	135.1	128.1	5.4 ($f = 0.25, \kappa_\lambda = 0.3034$)
	f_{Edd}	1	1	0.4
	$L_{bol,opt}$	9.069	8.936	0.883
	β		12	18
	T_{hi}		20000	35000
	T_{lo}		10000	14000
SDSS J0924+0219	χ^2_{min}	37.4	35.5	1.7 ($f = 0.16, \kappa_\lambda = 0.3233$)
	f_{Edd}	1	1	0.3
	$L_{bol,opt}$	1.263	1.261	0.035
	β		6	12
	T_{hi}		10000	25000
	T_{lo}		6000	12000
HE 1113–0641	χ^2_{min}	13.2	12.8	2.4 ($f = 0.36, \kappa_\lambda = 0.6448$)
	f_{Edd}	0.7	0.8	1
	$L_{bol,opt}$	0.699	0.798	0.197
	β		6	12
	T_{hi}		10000	35000
	T_{lo}		6000	16000
PG 1115+080	χ^2_{min}	62.3	65.8	2.7 ($f = 0.04, \kappa_\lambda = 0.1753$)
	f_{Edd}	1	1	1
	$L_{bol,opt}$	13.892	13.718	0.956
	β		3	18
	T_{hi}		15000	15000
	T_{lo}		10000	12000
RX J1131–1231	χ^2_{min}	34.2	23.7	14.6 ($f = 0.36, \kappa_\lambda = 0.7578$)
	f_{Edd}	0.3	0.4	0.2
	$L_{bol,opt}$	0.206	0.275	0.032
	β		6	12
	T_{hi}		10000	35000
	T_{lo}		6000	16000
SDSS J1138+0314	χ^2_{min}	53.8	53.5	29.7 ($f = 0.16, \kappa_\lambda = 0.3073$)
	f_{Edd}	1	1	1
	$L_{bol,opt}$	0.461	0.460	0.038
	β		6	12
	T_{hi}		10000	35000
	T_{lo}		6000	16000
WFI J2026–4536	χ^2_{min}	78.8	75.8	16.3 ($f = 0.25, \kappa_\lambda = 0.2972$)
	f_{Edd}	1	1	1
	$L_{bol,opt}$	8.956	8.851	1.327
	β		12	12
	T_{hi}		15000	25000
	T_{lo}		8000	12000
WFI J2033–4723	χ^2_{min}	299.4	300.0	111.0 ($f = 0.04, \kappa_\lambda = 0.1047$)
	f_{Edd}	1	1	1
	$L_{bol,opt}$	2.062	2.058	0.063
	β		6	6
	T_{hi}		10000	15000
	T_{lo}		6000	8000

T_{hi} , T_{lo} and β . We plot the resulting half-light radii vs. wavelength, SEDs, and χ^2_{min} values for each quasar individually in Figure 5; see the figure caption for details. We present the χ^2_{min} values and best-fit parameter values for the SS73, forming disc, and best-fit magnetically restrained models in Table 3. For ease of comparison with other size values, Table 2 presents I -band flux sizes r_I for both the $\beta = 3/4$ case and the best-fit magnetically restrained models, calculated following Appendix C.

The first point to notice about the best fits is that the best-fit SS73 and forming disc models usually have large f_{Edd} ($0.7 \leq f_{Edd} \leq 1$ in nine out of eleven cases). Larger f_{Edd} results in a larger accretion disc, making it easier to match the large inferred half-light radii. This effect is less pronounced in the best-fit magnetically restrained models; they have $f_{Edd}=1$ in six of eleven cases, but three of those are poor fits. (However, we have only considered face-on discs in our modelling. An inclined disc will have half-light radii smaller than it does when face-on, and given that quasar discs will have a nonzero average inclination angle, the true best-fit f_{Edd} of our objects in all models will, statistically, be somewhat larger than the values quoted.)

The second point to notice is that the forming disc model is never a significantly better fit than the SS73 model.

The third point to notice is that in eight of eleven cases, the magnetically restrained models can provide a fit which is better than the SS73 or forming disc fit and is also a statistically acceptable fit at the 99.73% confidence level if the full errors σ from B11 are used in the χ^2 calculations. (If the σ_r values are used instead, only in five of eleven cases are statistically acceptable fits found.)

Two of the cases without acceptable fits using σ , HE 0230 and WFI J2033, have unusual wavelength dependences of their half-light radii and are discussed below. The third case, SDSS J1138, has the lowest M_{BH} and the largest ratio of $L_{bol,opt}$ to M_{BH} in our sample. The SS73 and forming disc models can match the luminosity of SDSS J1138, but not its large half-light radii, even with $f_{Edd}=1$. The magnetically restrained models with $f_{Edd}=1$ can better match the shape of its half-light radius vs. wavelength curve, but still cannot match their large values, and is a worse fit to the observed luminosity. The large χ^2_{min} in this object could be reduced if future observations reveal that its M_{BH} is larger than the value we adopt, which is quite plausible given the considerable uncertainties on M_{BH} estimates (see, e.g., the comprehensive review of Shen 2013). The same might be true of HE 0230 and WFI J2033, which in addition to the unusual wavelength dependences of their half-light radii have the next largest ratios of $L_{bol,opt}$ to M_{BH} in our sample.

However, Table 2 shows that the flux sizes of the best-fit magnetically restrained models are still about an order of magnitude smaller, on average, than the measured microlensing sizes. (They are larger than the flux sizes of a $\beta = 3/4$ disc by $\Delta \log r_{1/2} = +0.37$ on average.) The one exception is HE 0230–2130, which has a best-fit magnetically restrained model with $f = 0$, corresponding to negligible thermal emission within the radius of the temperature spike. Except in that case, our best-fit magnetically restrained models produce more flux than observed in these objects. Incorporating flux sizes as a constraint in the fitting might shift the best-fit f values to $f = 0$ in many cases, as the χ^2 minimum as a function of f is quite broad.

The best-fit SS73 and forming disc models tend to overestimate $L_{bol,opt}$, while the best-fit magnetically restrained model tends to slightly underestimate it. Better constraints on the models might be obtainable by including multiwavelength SEDs for these quasars in the χ^2 fits, rather than just the total $L_{bol,opt}$. In the cases of HE 0230, PG 1115 and WFI J2033, such constraints would considerably increase the χ^2 of the best-fit magnetically restrained models; those best-fit models have SEDs that peak closer to 10^4 \AA than 10^3 \AA . It is not clear if a magnetically restrained model would still yield a low χ^2_{min} for PG 1115 if measurements of its multiwavelength SED were available for consideration in the fitting.

There are some similarities among the eight acceptable magnetically restrained model fits. Those best fits have $0.04 \leq f \leq 0.36$, corresponding to temperatures between 20% and 60% of the SS73 value. The best-fit β is 12 or 18, except for MG J0414 ($\beta = 3$). (Note that MG J0414 is also consistent with an SS73 or forming disc.) The best-fit T_{lo} is between 12000 K and 16000 K, again except for MG J0414 ($T_{lo}=28000$ K). The best-fit T_{hi} is between 25000 K and 35000 K, except for MG J0414 ($T_{hi}=60000$ K) and PG 1115 ($T_{hi}=15000$ K). The best-fit values of f_{Edd} , however, range from 0.03 to 1.

We can therefore characterize the best-fit temperature profile in seven of eleven cases as a magnetically restrained model with a temperature $(40 \pm 20)\%$ of the SS73 value within the radius where the SS73 disc reaches (14000 ± 2000) K, at which radius it has a temperature spike reaching (30000 ± 5000) K, which falls off as a power law $\propto R^{-(15 \pm 3)}$.

4.4.1 Quasars with half-light radii which decrease with increasing wavelength

Two quasars in B11 (HE 0230 and WFI J2033) appear to have half-light radii that decrease with increasing wavelength, albeit with large uncertainties. A temperature profile which increases with radius and then abruptly decreases can in principle reproduce the sign of this trend. (Conceptually, such a temperature profile might arise if the accretion luminosity is dominated by a shock at some radius R_b , with cooling gas undergoing radial infall within R_b .)

The two quasars above have maximum $\Delta \log r_{1/2} = -0.61 \pm 0.54$ and $\Delta \log r_{1/2} = -0.45 \pm 0.54$, respectively, from λ_{min} to λ_{max} . However, a radially inverted temperature profile like that described above cannot explain changes in $r_{1/2}$ greater than about $\Delta \log r_{1/2} \simeq -0.15$. That $\Delta \log r_{1/2}$ corresponds to the case of a narrow temperature spike at $r_{1/2}(\lambda_{min})$ which generates all the luminosity at λ_{min} , and a flat temperature profile within that radius which dominates the luminosity observed at λ_{max} , yielding $r_{1/2}(\lambda_{max}) = \frac{1}{\sqrt{2}} r_{1/2}(\lambda_{min})$, so that $\Delta \log r_{1/2} = -\log \sqrt{2} \simeq -0.15$. A temperature profile increasing with radius within $r_{1/2}(\lambda_{min})$ will produce an even smaller $\Delta \log r_{1/2}$ value. A temperature profile decreasing with radius within $r_{1/2}(\lambda_{min})$ before spiking to a high temperature at that radius will not match the observed smooth change in $r_{1/2}$ with wavelength; such a temperature profile would yield $r_{1/2}$ values decreasing and then increasing with wavelength.

B11 note that the anomalous wavelength dependence of

these two objects' size estimates might also be produced by unusual microlensing caustic patterns such as those found at the center of an astroid caustic. (The magnification increases away from the center of an astroid caustic, leading to larger flux anomalies for larger sources.) That explanation for these objects' half-light radii seems more likely after consideration of the difficulty in reproducing the results with actual disc temperature profiles. We predict that further observations of these two objects will not show the anomalous size estimates, as long as the time baseline between old and new observations is sufficient for the unusual microlensing caustic pattern to have moved out of our line of sight to the continuum source.

5 DISCUSSION AND CONCLUSIONS

We have tested several energetically plausible quasar accretion disc temperature profile models against the large quasar accretion disc half-light radii inferred by B11 from microlensing observations.

We have shown that the temperature profiles from our toy model of the torn accretion discs proposed by NKPF are not able to simultaneously match observed quasar SEDs and the microlensing sizes of B11. In our toy model, torn discs yield precessing rings of gas orbiting at supersonic speeds which shock when they intersect and yield SEDs which are much bluer than observed quasar SEDs.

We have demonstrated that acceptable fits (at the 3σ level) to the half-light radii of B11 — in other words, theory sizes matching the microlensing sizes — can be found in eight of eleven cases for model discs with a temperature spike at some radius and lowered temperatures within that radius (our magnetically restrained models). Acceptable fits can be found in only four of eleven cases for discs with normal SS73 temperature profiles and in only three of eleven cases for discs with normal temperature profiles inside a temperature spike (our forming disc models). The poor χ^2_{min} for both forming disc models and magnetically restrained models with large f indicate that the shape of the temperature profile outside the temperature spike is not a major factor in obtaining an acceptable fit.

We find that the best-fit temperature profile in seven of eleven cases is a magnetically restrained model with a temperature $(40\pm 20)\%$ of the SS73 value within the radius where the SS73 disc reaches (14000 ± 2000) K, at which radius it has a temperature spike reaching (30000 ± 5000) K, which falls off as a power law $\propto R^{-(15\pm 3)}$.

However, such profiles do not produce flux sizes as large as their theory sizes, by about an order of magnitude. Constraining the magnetically restrained models to explicitly match the flux sizes may produce better fits by reducing the best-fit f values.

We note that the two quasars in B11 which have half-light radii that appear to decrease with increasing wavelength cannot be fully explained by a radially increasing temperature profile with an abrupt cutoff. They must instead be examples of unusual microlensing patterns; e.g., astroid caustics (§ 4.4.1).

Future progress on the issue of quasar accretion disc temperature profiles will require additional and improved observations and modelling. Measurements of the wave-

length dependence of half-light radii in lensed quasars could be expanded to larger samples and extended to shorter wavelengths using the Hubble Space Telescope. Improved M_{BH} estimates for gravitationally lensed quasars would yield better constraints on models providing acceptable fits to half-light radii, as would multiwavelength SED measurements (such as photometrically calibrated flux measurements of lens images at observed optical and infrared wavelengths). One worthwhile improvement to the modelling would be to self-consistently use the luminosity profiles which have here been found to provide good fits to the half-light radii as input to simulations of the microlensing flux deviations. Currently the simulations use elliptical Gaussians, whereas at high temperatures the best-fit profiles found here will resemble elliptical rings on the sky.

Further exploration of model temperature profiles consistent with improved observations could then follow. Models with $f_{Edd}>1$ and super-Eddington luminosities (e.g., Abramowicz et al. 1988) may be worth considering, as the best-fit models we find here tend to cluster at our imposed limit of $f_{Edd}=1$. Also, each of our magnetically restrained models has an angular velocity which is a fixed fraction f of the Keplerian value, but a more general extension of the models of Ogilvie (1997) would involve a power-law dependence of the angular velocity on radius ($f \equiv (R/R_b)^x$), arising from an assumed radial power-law dependence of the magnetic field strength.

Eventually, such parametric modelling should be superseded by the use of temperature profiles from theoretical simulations of accretion discs. If the results of B11 are borne out by further observations, a strong test of such simulations will be how naturally they can generate the temperature profiles allowed by observations.

Alternatively, if future observations rule out the possibility that quasar accretion discs have flat temperature profiles, inhomogeneous accretion discs (Dexter & Agol 2011) offer a potential solution to the discrepancy between microlensing and flux sizes. Inhomogeneous discs simultaneously increase the radius within which emission at a given wavelength occurs (increasing the microlensing size) and decrease the area within that radius which emits at that wavelength (increasing the flux size).

ACKNOWLEDGEMENTS

We thank C. Kochanek for valuable comments. PBH thanks NSERC for research support for LSC and EW. ESN thanks NSERC for an Undergraduate Student Research Award. CJN acknowledges support provided by NASA through the Einstein Fellowship Program, grant PF2-130098.

References

- Abolmasov P., Shakura N. I., 2012, MNRAS, 427, 1867
- Abramowicz M. A., Czerny B., Lasota J. P., Szuszkiewicz E., 1988, Astrophys. J., 332, 646
- Bardeen J. M., Petterson J. A., 1975, Astrophys. J. Lett., 195, L65
- Bate N. F., Floyd D. J. E., Webster R. L., Wyithe J. S. B., 2008, MNRAS, 391, 1955

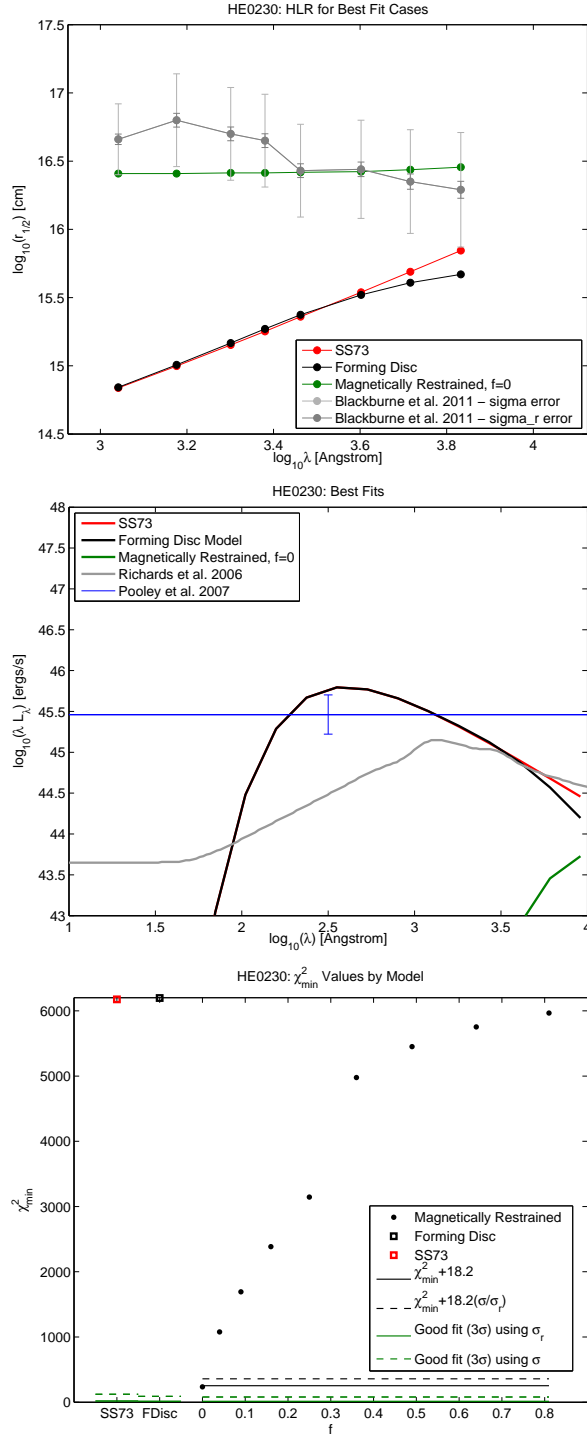


Figure 5. Half-light radius $r_{1/2}$ vs. wavelength (top row), spectral energy distribution (middle row), and χ^2_{min} results (bottom row) for each of the quasars studied. In the $r_{1/2}$ plots, the measured points from B11 are shown in grey, with the random and full errors on each $r_{1/2}$ value shown as the shorter and longer error bars, respectively. The best-fit SS73 model is shown in red, the best-fit forming disc model in black, and the best-fit magnetically restrained model in green. In the SED plots, the quasar's $L_{bol,opt}$ value from Pooley et al. (2007) is shown as the horizontal blue line. The mean SED from Richards et al. (2006), summed from 10^2 \AA to 10^4 \AA , is normalized to that value as a reference for the typical shape of a quasar's ultraviolet/optical SED. In the χ^2_{min} plots, the red open square on the left shows the SS73 disc χ^2_{min} , the black open square next to it shows the forming disc χ^2_{min} , and the circles show the χ^2_{min} for the magnetically restrained disc model at each value of f tested. The solid green line segments show, for each model, the upper limit for a statistically acceptable fit at the 99.73% (3σ) confidence level, using the random errors only. The dashed green line segments show the same upper limit using the full errors quoted in B11. For the magnetically restrained models, we use black lines to show the 3σ confidence limits for the five free parameters of the model ($\Delta\chi^2 \leq 18.2$): at 99.73% confidence, magnetically restrained models underneath the black lines provide fits as statistically acceptable as the best fit found, using random errors only (solid black line) or the full errors from B11 (dashed black line). Note that we plot confidence limits for all five free parameters, not just one free parameter, because the best-fit magnetically restrained models as a function of f typically have differing values of the other parameters.

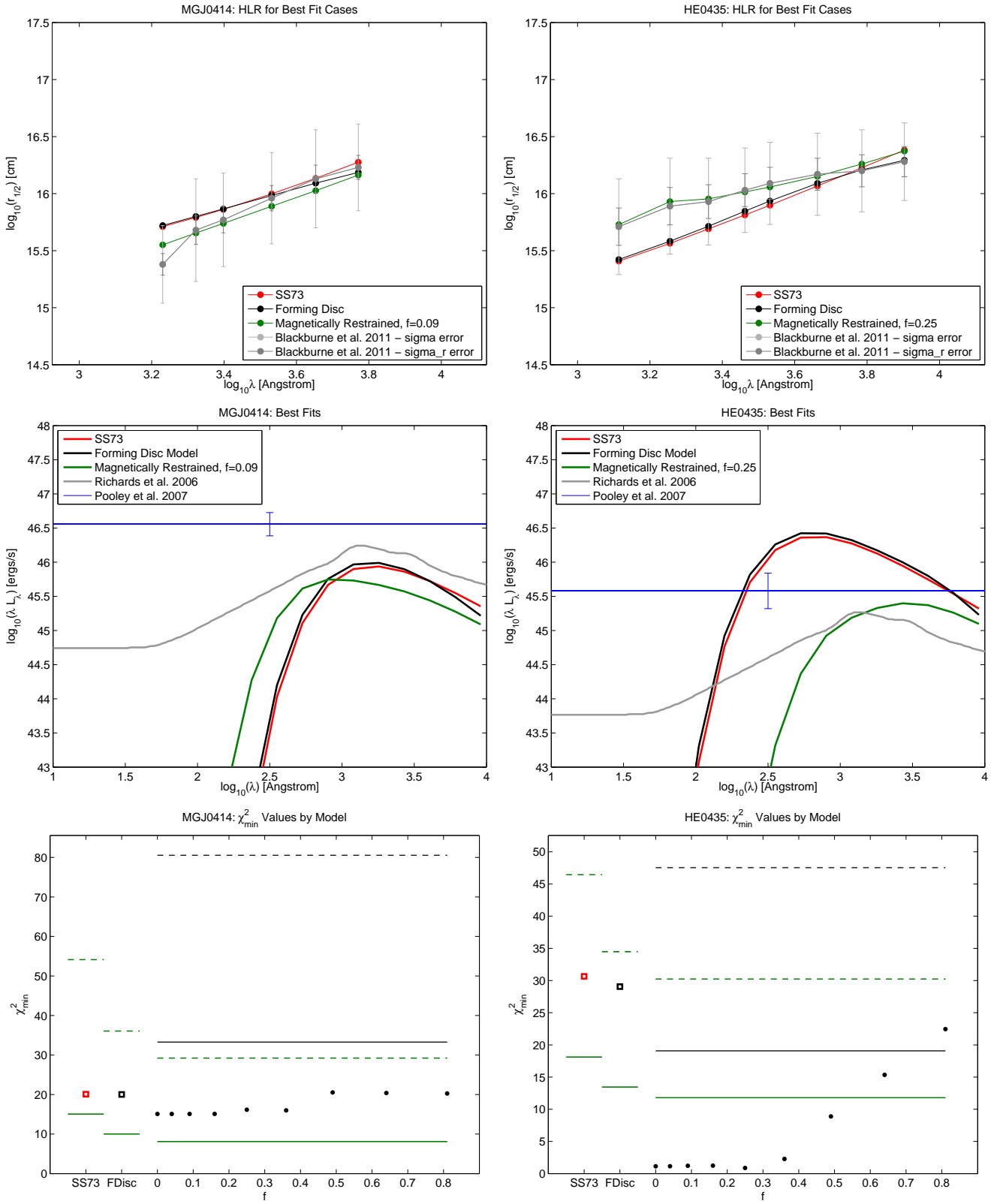


Figure 5 – continued

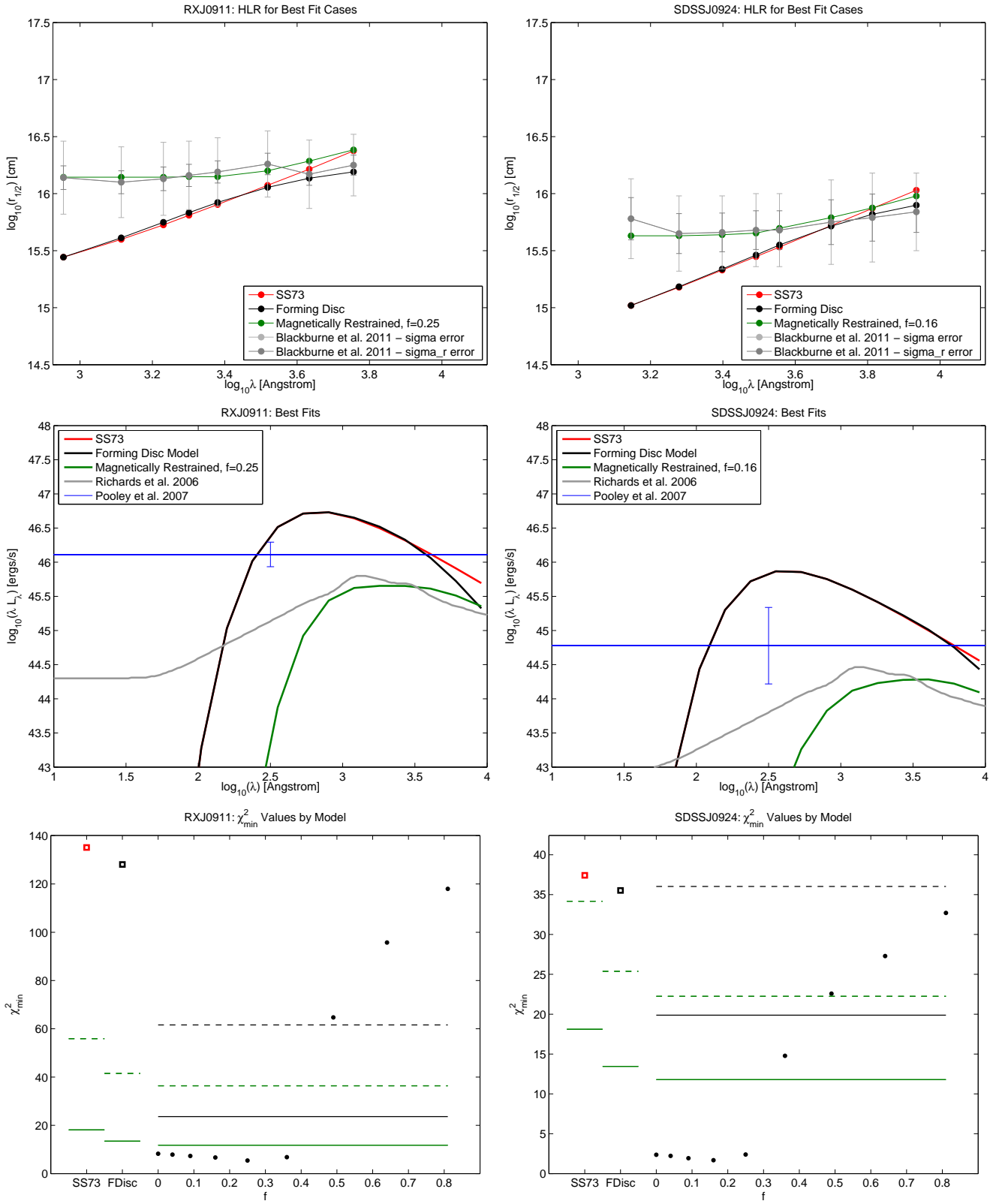


Figure 5 – continued

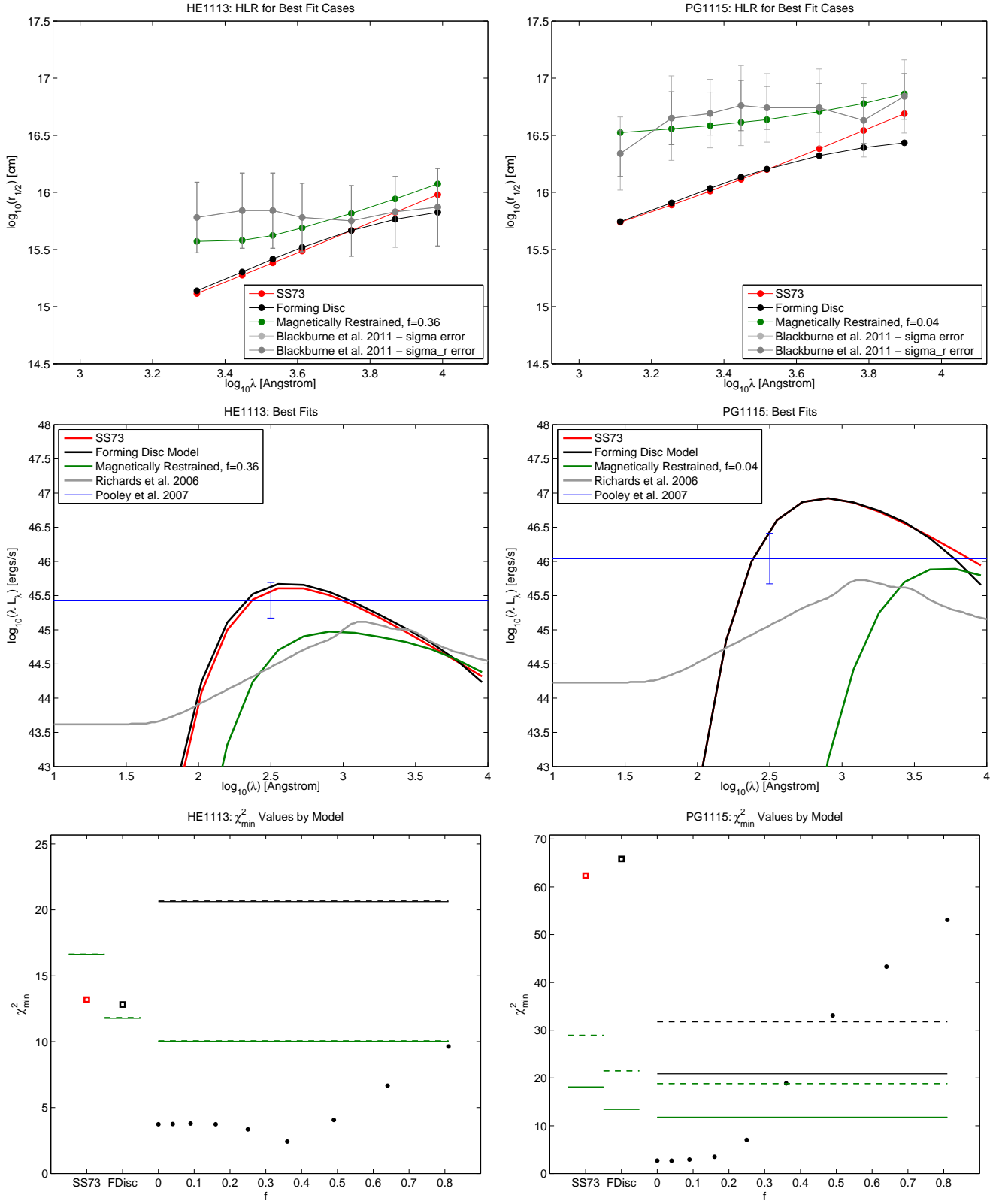


Figure 5 – continued

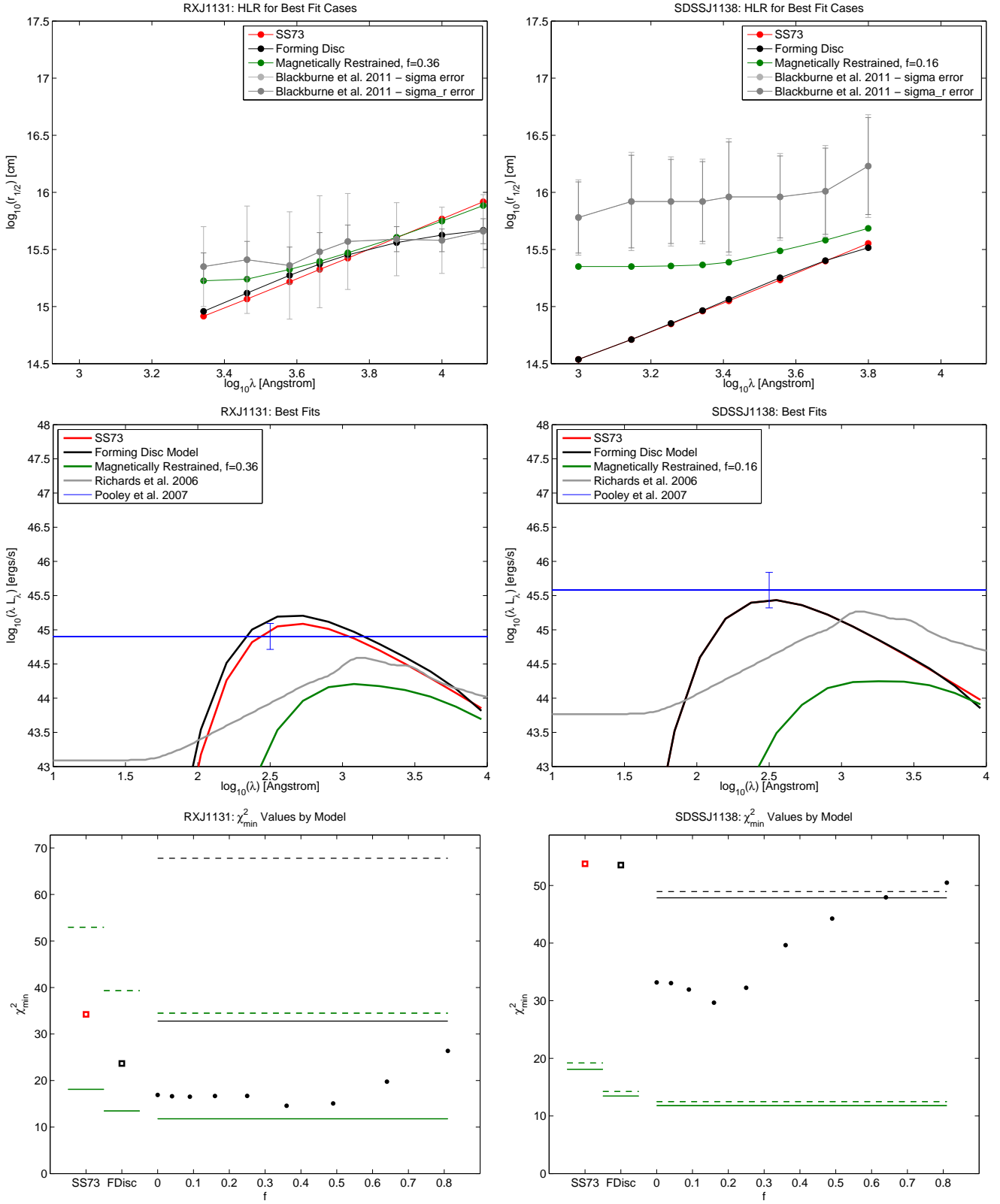


Figure 5 – continued

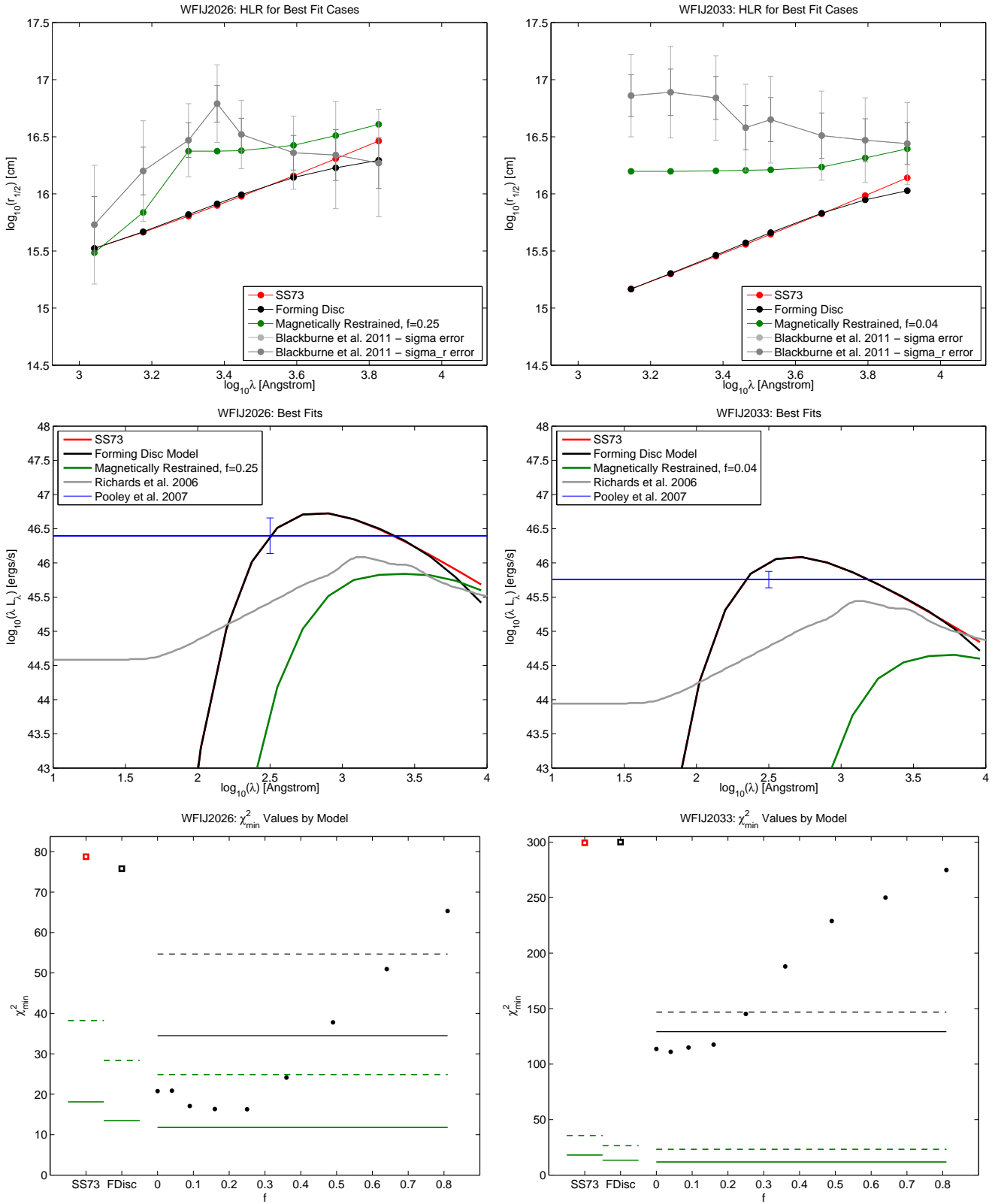


Figure 5 – continued

Blackburne J. A., Pooley D., Rappaport S., Schechter P. L., 2011, *Astrophys. J.*, 729, 34

Bonning E. W., Shields G. A., Stevens A. C., Salviander S., 2013, *Astrophys. J.*, 770, 30

Dai X., Kochanek C. S., Chartas G., Kozłowski S., Morgan C. W., Garmire G., Agol E., 2010, *Astrophys. J.*, 709, 278

Dexter J., Agol E., 2011, *ApJL*, 727, L24

Eigenbrod A., Courbin F., Meylan G., Agol E., Anguita T., Schmidt R. W., Wambsganss J., 2008, *Astron. Astrophys.*, 490, 933

Floyd D. J. E., Bate N. F., Webster R. L., 2009, *MNRAS*, 398, 233

Jiménez-Vicente J., Mediavilla E., Muñoz J. A., Kochanek C. S., 2012, *Astrophys. J.*, 751, 106

King A. R., Pringle J. E., 2006, *Mon. Not. R. Astron. Soc.*, 373, L90

—, 2007, *Mon. Not. R. Astron. Soc.*, 377, L25

Kollmeier J. A., Onken C. A., Kochanek C. S., Gould A., Weinberg D. H., Dietrich M., Cool R., Dey A., Eisenstein D. J., Jannuzi B. T., Le Floc'h E., Stern D., 2006, *Astrophys. J.*, 648, 128

Kumar S., Pringle J. E., 1985, *MNRAS*, 213, 435

Lense J., Thirring H., 1918, *Physikalische Zeitschrift*, 19, 156

Lubow S. H., Ogilvie G. I., Pringle J. E., 2002, *MNRAS*, 337, 706

Mediavilla E., Muñoz J. A., Kochanek C. S., Guerras E., Acosta-Pulido J., Falco E., Motta V., Arribas S., Manchado A., Mosquera A., 2011, *Astrophys. J.*, 730, 16

Morgan C. W., Hainline L. J., Chen B., Tewes M., Kochanek C. S., Dai X., Kozłowski S., Blackburne J. A., Mosquera A. M., Chartas G., Courbin F., Meylan G., 2012, *Astrophys. J.*, 756, 52

Morgan C. W., Kochanek C. S., Dai X., Morgan N. D., Falco E. E., 2008, *Astrophys. J.*, 689, 755

Morgan C. W., Kochanek C. S., Morgan N. D., Falco E. E., 2010, *Astrophys. J.*, 712, 1129

Mosquera A. M., Kochanek C. S., 2011, *Astrophys. J.*, 738, 96

Mosquera A. M., Muñoz J. A., Mediavilla E., Kochanek C. S., 2011, *Astrophys. J.*, 728, 145

Narayan R., Igumenshchev I. V., Abramowicz M. A., 2003, *Publ. Astron. Soc. Jpn.*, 55, L69

Nayakshin S., 2005, *Mon. Not. R. Astron. Soc.*, 359, 545

Nixon C., King A., Price D., Frank J., 2012a, *Astrophys. J. Lett.*, 757, L24

Nixon C. J., King A. R., Price D. J., 2012b, *MNRAS*, 422, 2547

Novikov I. D., Thorne K. S., 1973, in *Black Holes (Les Astres Occlus)*, Dewitt C., Dewitt B. S., eds., pp. 343–450

Ogilvie G. I., 1997, *MNRAS*, 288, 63

—, 1999, *MNRAS*, 304, 557

Papaloizou J. C. B., Lin D. N. C., 1995, *Astrophys. J.*, 438, 841

Papaloizou J. C. B., Pringle J. E., 1983, *MNRAS*, 202, 1181

Poindexter S., Kochanek C. S., 2010, *Astrophys. J.*, 712, 668

Poindexter S., Morgan N., Kochanek C. S., 2008, *Astrophys. J.*, 673, 34

Pooley D., Blackburne J. A., Rappaport S., Schechter P. L., 2007, *Astrophys. J.*, 661, 19

Pringle J. E., 1992, *MNRAS*, 258, 811

Richards G. T., Lacy M., Storrie-Lombardi L. J., Hall P. B., Gallagher S. C., Hines D. C., Fan X., Papovich C., Vanden Berk D. E., Trammell G. B., Schneider D. P., Vestergaard M., York D. G., Jester S., Anderson S. F., Budavári T., Szalay A. S., 2006, *ApJS*, 166, 470

Sazonov S. Y., Ostriker J. P., Sunyaev R. A., 2004, *MNRAS*, 347, 144

Scott A. E., Stewart G. C., Mateos S., 2012, *Mon. Not. R. Astron. Soc.*, 423, 2633

Shakura N. I., Sunyaev R. A., 1973, *A&A*, 24, 337

Shen Y., 2013, *Bulletin of the Astronomical Society of India*, 41, 61

Sutton A. D., Roberts T. P., Middleton M. J., 2013, *ArXiv e-prints*

Tremaine S., Davis S. W., 2013, *ArXiv e-prints*

Wambsganss J., 2006, in *Saas-Fee Advanced Course 33: Gravitational Lensing: Strong, Weak and Micro*, Meylan G., Jetzer P., North P., Schneider P., Kochanek C. S., Wambsganss J., eds., pp. 453–540

APPENDIX A: FORMING DISC MODEL CONSTRAINTS

The energy per second emitted from the disc in its forming region ($R > R_b$) must satisfy $L \leq \frac{1}{2}GM\dot{M}_{BH}/R_b$ (see §4.1).

Considering both sides of the disc,

$$2 \int_{R_b}^{\infty} \sigma_{sb} [T_{\text{surf}}(R)]^4 dA \leq \frac{GM_{BH}\dot{M}}{2R_b} \quad (\text{A1})$$

Writing $T_{\text{surf}}(R) = T_{hi}(R/R_b)^{-\beta}$ at $R \geq R_b$, with $\beta > \frac{1}{2}$, we have

$$2 \int_{R_b}^{\infty} \sigma_{sb} T_{hi}^4 (R/R_b)^{-4\beta} 2\pi R dR \leq \frac{GM_{BH}\dot{M}}{2R_b} \quad (\text{A2})$$

$$4\pi R_b^2 \sigma_{sb} T_{hi}^4 \int_{R_b}^{\infty} (R/R_b)^{-4\beta} R/R_b d(R/R_b) \leq \frac{GM_{BH}\dot{M}}{2R_b} \quad (\text{A3})$$

Making the substitution $x = R/R_b$,

$$4\pi R_b^2 \sigma_{sb} T_{hi}^4 \int_1^{\infty} x^{-4\beta+1} dx \leq \frac{GM_{BH}\dot{M}}{2R_b} \quad (\text{A4})$$

$$4\pi R_b^2 \sigma_{sb} T_{hi}^4 \frac{1}{4\beta - 2} \leq \frac{GM_{BH}\dot{M}}{2R_b} \quad (\text{A5})$$

$$\sigma_{sb} T_{hi}^4 \leq \left[\beta - \frac{1}{2} \right] \frac{GM_{BH}\dot{M}}{2\pi R_b^3} \quad (\text{A6})$$

APPENDIX B: MAGNETICALLY RESTRAINED DISC MODEL CONSTRAINTS

In our magnetically restrained disc models, gas accreting through a Keplerian disc at large radii is presumed to reduce its orbital velocity to a fraction $f < 1$ of its Keplerian value by the time it reaches radius R_b . The disc thus has a fraction $(1 - f^2)$ of the kinetic energy of the accreting gas at R_b available to emit as heat at $R > R_b$, in addition to the normal disc emission ($\propto T_{SS73}^4$) at $R > R_b$.

Consider a disc obeying $T_{\text{surf}}(R) = T_{hi}(R/R_b)^{-\beta}$ from $R_b \leq R \leq R_c$ and a normal SS73 $T_{\text{surf}}(R) = T_{lo}(R/R_b)^{-3/4}$ profile at $R > R_c$, where $T_{hi}(R_c/R_b)^{-\beta} \equiv T_{lo}(R_c/R_b)^{-3/4}$ so that $T_{lo}/T_{hi} = (R_c/R_b)^{-\beta+3/4}$ and $(R_c/R_b) = (T_{lo}/T_{hi})^{\frac{1}{-\beta+3/4}}$.

We have a limit on the excess energy emitted by the disc, which is equal to the total energy emitted by the disc minus the energy that would have been emitted by an SS73 disc between those radii. Again considering both sides of the disc,

$$2 \int_{R_b}^{R_c} \sigma_{sb} T_{hi}^A (R/R_b)^{-4\beta} dA - 2 \int_{R_b}^{R_c} \sigma_{sb} T_{lo}^A (R/R_b)^{-3} dA \leq (1-f^2) \frac{GM_{BH} \dot{M}}{2R_b} \quad (\text{B1})$$

Expanding dA and making the substitution $x = R/R_b$,

$$4\pi R_b^2 \sigma_{sb} T_{hi}^A \left[\int_1^{R_c/R_b} x^{-4\beta+1} dx - \int_1^{R_c/R_b} \frac{T_{lo}^A}{T_{hi}^A} x^{-2} dx \right] \leq (1-f^2) \frac{GM_{BH} \dot{M}}{2R_b} \quad (\text{B2})$$

which evaluates to

$$4\pi R_b^2 \sigma_{sb} T_{hi}^A \left[\frac{x^{-4\beta+2}}{-4\beta+2} \Big|_1^{R_c/R_b} + \left(\frac{T_{lo}}{T_{hi}} \right)^4 \frac{x^{-3}}{3} \Big|_1^{R_c/R_b} \right] \leq (1-f^2) \frac{GM_{BH} \dot{M}}{2R_b} \quad (\text{B3})$$

Defining $t_{lh} \equiv T_{lo}/T_{hi}$, we have:

$$4\pi R_b^2 \sigma_{sb} T_{hi}^A \left[\frac{1}{-4\beta+2} \left(t_{lh}^{\frac{4\beta-2}{\beta-3/4}} - 1 \right) + \frac{1}{3} \left(t_{lh}^{\frac{4\beta}{\beta-3/4}} - t_{lh}^4 \right) \right] \leq (1-f^2) \frac{GM_{BH} \dot{M}}{2R_b} \quad (\text{B4})$$

Examining the above equation, we see that for it to be satisfied in the limit $f \rightarrow 1$, where no excess energy is available, then we must have $t_{lh} \rightarrow 1$, or $T_{hi} = T_{lo}$, as expected.

Thus, the constraint on our magnetically restrained disc models is given by:

$$\sigma_{sb} T_{hi}^A \leq (1-f^2) \frac{GM_{BH} \dot{M}}{8\pi R_b^3} \Big/ \left[\frac{1}{-4\beta+2} \left(t_{lh}^{\frac{4\beta-2}{\beta-3/4}} - 1 \right) + \frac{1}{3} \left(t_{lh}^{\frac{4\beta}{\beta-3/4}} - t_{lh}^4 \right) \right] \quad (\text{B5})$$

where $t_{lh} \equiv T_{lo}/T_{hi}$.

APPENDIX C: ACCRETION DISC FLUX SIZES

The *flux size* of a quasar accretion disc (M10) is found by using the quasar's observed flux to calculate its luminosity and determining the size a standard SS73 disc would need to be to generate that luminosity.

Given a lensed quasar's demagnified apparent magnitude I , the flux size in the I band ($\lambda_{I,obs} = 0.814 \mu\text{m}$) for the accretion disc of that quasar, located at angular size distance D_{OS}/r_H (in units of the Hubble radius $r_H = c/H_0$) with inclination i and with a temperature profile $T(R) \propto R^{-\beta}$, is given by:

$$R_I = \frac{2.83 \times 10^{15}}{\sqrt{K_\lambda(\beta) \cos i}} \left(\frac{D_{OS}}{r_H} \right) \left(\frac{\lambda_{I,obs}}{\mu\text{m}} \right)^{3/2} 10^{-0.2(I-19)} h^{-1} \text{ cm} \quad (\text{C1})$$

where $H_0 = 100h \text{ km s}^{-1} \text{ Mpc}^{-1}$ and where

$$K_\lambda(\beta) = \frac{1}{2.58} \int_0^\infty u du [\exp(u^\beta) - 1]^{-1} \quad (\text{C2})$$

is the integral over the disc surface brightness, normalized to unity for $\beta = 3/4$.

The $K_\lambda(\beta)$ integral is obtained as follows. For observations at rest wavelength λ , we can write $T(R) = T_\lambda(R/R_\lambda)^{-\beta}$, with $T_\lambda \equiv hc/k\lambda$ and

$$R_\lambda \equiv \frac{1}{\pi^2} \left(\frac{45 \lambda^4 R_g \dot{M}}{16 h_p} \right)^{1/3} \quad (\text{C3})$$

where $R_g = GM_{BH}/c^2$. We then have

$$K_\lambda(\beta) \propto \int_0^\infty R dR [\exp(hc/k\lambda T(R)) - 1]^{-1} \quad (\text{C4})$$

$$\propto \int_0^\infty R dR [\exp(R^\beta/R_\lambda^\beta) - 1]^{-1} \quad (\text{C5})$$

$$\propto R_\lambda^2 \int_0^\infty u du [\exp(u^\beta) - 1]^{-1} \quad (\text{C6})$$

where we have defined $u \equiv R/R_\lambda$.

In the case of our magnetically restrained models (§ 4.2), where the disc temperature profile has three parts, we can generalize $K_\lambda(\beta)$ to $\kappa_\lambda(\beta, f, T_{lo}, T_{hi})$:

$$\kappa_\lambda(\beta, f, T_{lo}, T_{hi}) \propto \left[\int_0^{u_1} \frac{R_\lambda^2 u du}{\exp(u^{3/4}/\sqrt{f}) - 1} + \int_{u_1}^{u_2} \frac{R_\lambda^2 u du}{\exp(gu^\beta) - 1} + \int_{u_2}^\infty \frac{R_\lambda^2 u du}{\exp(u^{3/4}) - 1} \right] \quad (\text{C7})$$

where $u \equiv R/R_\lambda$ as before. In the equation above, we define $u_1 \equiv R_b/R_\lambda$ and $u_2 \equiv R_c/R_\lambda$, with R_b and R_c as defined in § 4.2, and we define $g \equiv (T_\lambda/T_{hi})(R_\lambda/R_b)^\beta$. The constant of proportionality is the same for $K_\lambda(\beta)$ and $\kappa_\lambda(\beta, f, T_{lo}, T_{hi})$, so the ratio of those two quantities gives the ratio of the flux sizes for an SS73 model disc and a magnetically arrested one.